

# Structural and Thermodynamic Properties of Magnesium-rich Liquids at Ultrahigh Pressure

Felipe González-Cataldo<sup>1</sup>  and Burkhard Militzer<sup>1,2</sup>

<sup>1</sup> Department of Earth and Planetary Science, University of California, Berkeley, CA 94720, USA; f\_gonzalez@berkeley.edu

<sup>2</sup> Department of Astronomy, University of California, Berkeley, CA 94720, USA; militzer@berkeley.edu

\* Correspondence: f\_gonzalez@berkeley.edu

**Abstract:** We explore the structural properties of Mg, MgO and MgSiO<sub>3</sub> liquids from *ab initio* computer simulations at conditions are relevant for the interiors of giant planets, stars, shock compression measurements and inertial confinement fusion experiments. Using path integral Monte Carlo and density functional theory molecular dynamics, we derive the equation of state of magnesium-rich liquids in the regime of condensed and warm dense matter, with densities ranging from 0.32 to 86.11 g cm<sup>-3</sup> and temperatures from 20 000 K to 5×10<sup>8</sup> K. We study the electronic structure of magnesium as a function of density and temperature and the correlations of the atomic motion. We find an unexpected local maximum in the pair correlation functions that emerges at high densities, which decreases the coordination number of elemental magnesium and reveals a higher packing. We do not observe this phenomenon in other magnesium liquids that maintain a rather constant coordination number.

**Keywords:** density functional theory, silicates, coordination number

## 1. Introduction

Magnesium-rich liquids are significant minerals in planetary science because they represent the main constituent of magma oceans [1] that formed when iron and silicates phase separated during the formation of Earth and super-Earth planets [2–4]. Sizable magma oceans have been predicted to persist over long periods of time [5]. Understanding how the properties magnesium-rich liquids change with pressure and temperature will thus enable us to better constrain the models of formation and evolution of rocky planets [6]. Magnesium-rich liquids also provide valuable information for inertial confinement fusion (ICF) experiments, where materials are exposed to extreme conditions [7–9] that transform liquids into warm dense matter and dense plasmas that are difficult to understand. State-of-the-art laboratories, including the National Ignition Facility (NIF) at Lawrence Livermore National Laboratory, the Omega laser at the University of Rochester, the Z machine at Sandia National Laboratory, and the SLAC laboratory, regularly investigate these conditions to explore matter in the high-energy density regime, exploring matter in the high-energy density regime by probing materials at ultrahigh pressure and temperature conditions never explored before, but that are present at the interior of white dwarf stars [10], rocky exoplanets [11,12], and giant planets like Jupiter [13,14]. While these experiments have accessed the warm dense matter regime and were able to achieve fusion conditions recently [15], theoretical methods have difficulties accessing this regime due to the strong level of ionization, which makes interpretation of experimental measurements a hard task.

The properties of magnesium-rich liquids are very interesting. Their Grüneisen parameter increases upon compression [16] and the heat capacity can increase beyond the ideal gas limit upon ionization [17]. MgO, SiO<sub>2</sub> and MgSiO<sub>3</sub> are all insulators in the solid phase but they all become modest electrical conductors in liquid form at high enough

**Citation:** González-Cataldo, F.; Militzer, B. Title. *Minerals* **2023**, *1*, 0. <https://doi.org/>

Received:

Revised:

Accepted:

Published:

**Copyright:** © 2023 by the authors. Submitted to *Minerals* for possible open access publication under the terms and conditions of the Creative Commons Attribution (CC BY) license (<https://creativecommons.org/licenses/by/4.0/>).

temperature and pressure, which implies that super-Earth planets can generate magnetic fields in their mantle [5,18]. The structure of liquid magnesiosilicates varies substantially with compression [19–21]. Some melts, such as  $\text{MgSiO}_3$ , are good solvents for water. The solubility was found to increase with pressure, which has important consequences for the Earth's mantle [22]. At high temperatures, it is also important to identify the thermal and pressure ionization regimes [23], as they modify the properties of the liquid as it becomes partially ionized. Recent *ab initio* calculations predicted mixed coordination numbers for silica between the 6-fold coordinated pyrite-type phase and the 9-fold coordinated  $\text{Fe}_2\text{P}$ -type phase at high pressure, as well as the formation of superoxides such as  $\text{SiO}_3$  and  $\text{SiO}_6$ , which may exist in the mantle of super-Earth planets [24].

In this study, we perform *ab initio* simulations of the liquids Mg, MgO, and  $\text{MgSiO}_3$  using a combination of density functional theory molecular dynamics (DFT-MD) and path integral Monte Carlo (PIMC), providing a detailed characterization of the structure of the liquids.

## 2. Simulation methods

Rigorous discussions of the PIMC [25–27] and DFT-MD [28–30] methods have been provided in previous works, and the details of our simulations have been presented in some of our previous publications [17,31–33]. Following earlier publications on hydrogen and helium, PIMC and DFT-MD simulations have been combined to study the properties of materials with core electrons in the regime of warm dense matter such as lithium fluoride [34], boron [35], aluminum [31], oxygen [36], silicon [37,38], hydrocarbons [38,39], and superionic water [40,41]. However, the structure of magnesium liquids has not been explored in detail in this regime of extreme conditions. We combine PIMC [42] and DFT-MD simulations as implemented in the Vienna Ab initio Simulation Package (VASP) [43] to generate a consistent Equation of State (EOS) for Mg, MgO, and  $\text{MgSiO}_3$  that spans across a wide range of ultrahigh temperatures and pressures.

For DFT-MD simulations, we employ Kohn-Sham DFT simulation techniques as implemented in the Vienna Ab initio Simulation Package (VASP) [43] using the projector augmented-wave (PAW) method [44,45], and molecular dynamics is performed in the NVT ensemble, regulated with a Nosé thermostat. The time step was adapted to the density and the temperature, ranging from 0.16 to 0.44 fs for simulation times from 1000 to 16 000 time steps, to ensure a reliable estimation of the thermodynamic quantities. The pseudopotentials used in our DFT-MD calculations freeze the electrons of the 1s orbital (He-core), which leaves 10, 12, and 6 valence electrons for Mg, Si, and O atoms, respectively. Exchange-correlation effects are described using the Perdew, Burke, and Ernzerhof [46] (PBE) generalized gradient approximation (GGA). However, for elemental Mg, the provided Mg PBE pseudopotential did not give proper results for high densities, so we switched to the local density approximation (LDA). We proceed in a similar way with MgO, the highest densities were also simulated using the LDA functional. As shown in Ref. [47], the choice of the pseudopotential in *ab initio* simulations of Mg has very little effects on the computed thermodynamic properties. We obtain a very good agreement between both functionals for a number of densities. Electronic wave functions are expanded in a plane-wave basis with a energy cut-off as high as 7000 eV in order to converge total energy. Size convergence tests with up to a 65-atom simulation cell at temperatures of 10 000 K and above indicate that pressures are converged to better than 0.6%, while internal energies are converged to better than 0.1%. We find, at temperatures above 500 000 K, that 15-atom supercells are sufficient to obtain converged results for both energy and pressure, since the kinetic energy far outweighs the interaction energy at such high temperatures [31,48]. The number of bands in each calculation was selected such that orbitals with occupation as low as  $10^{-4}$  were included, which requires up to 14 000 bands in an 15-atom cell at  $2 \times 10^6$  K and two-fold compression. All simulations are performed at the  $\Gamma$  point of the Brillouin zone, which is sufficient for high temperature fluids, converging total energy to better than 0.01% compared to a grid of  $k$ -points.

### 3. Results

In this section, provide a detailed characterization of the magnesium-rich liquids that we have obtained from our *ab initio* simulations of Mg [33], MgO [32], and MgSiO<sub>3</sub> [17], spanning the condensed matter, warm dense matter and plasma regimes. Computations were performed for a series of densities and temperatures ranging from 0.321–86.11 g cm<sup>-3</sup> and 10<sup>4</sup>–10<sup>8</sup> K. The full range of our EOS data points is shown in temperature-density and pressure-density space in Fig. 1, along with the shock Hugoniot curve of each material.

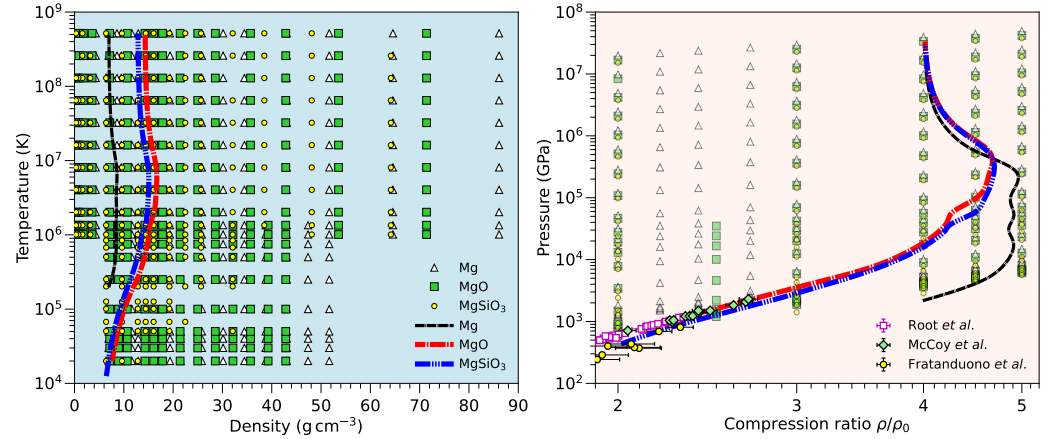


**Figure 1.** Temperature-density conditions of our PIMC and DFT-MD simulations. The thick dashed lines correspond to the shock Hugoniot curves that we derived for Mg, MgO, and MgSiO<sub>3</sub>, with initial densities  $\rho_0 = 1.736 \text{ g cm}^{-3}$ ,  $3.570 \text{ g cm}^{-3}$ ,  $3.208 \text{ g cm}^{-3}$ , respectively. The full EOS for each material is available in Refs [17,23,32,49]. Shock Experiments on MgO from McCoy *et al.* [50], and Root *et al.* [51], and shock experiments on MgSiO<sub>3</sub> from Fratanduno *et al.* [52], are included for comparison.

The ideal mixing approximation has been shown to perform well for temperatures above 10<sup>5</sup> K. [53], and the magnitude of nonideal mixing effects was found to be small in this regime, leading to shock Hugoniot curves of MgO and MgSiO<sub>3</sub> that are reproduced with sufficient accuracy by combining the EOSs of the elemental substances with the additive volume rule. This concept was extended to other mixtures [49] and good agreement the shock Hugoniot curves of H<sub>2</sub>O and CO<sub>2</sub> was found between laboratory measurements and theoretical predictions based on the linear mixing approximation. However, this approximation breaks down at lower temperatures, where chemical bonds play an increasingly important role. These bonds change the structure of the liquid, modifying the atomic coordination. Here we will study how the structure of the liquid changes with density and temperature. We will demonstrate that coordination of magnesium ions is sensitive to presence of silicon and oxygen.

#### 3.1. Radial Distribution Function

The atomic trajectories obtained from DFT-MD simulations can be used to study the local structure of the liquids. Using the radial distribution function, defined by

$$g_{\alpha\beta}(r) \equiv \frac{V}{4\pi r^2 N_\alpha N_\beta} \left\langle \sum_{i=1}^{N_\alpha} \sum_{j \neq i}^{N_\beta} \delta(r - \|\vec{r}_{ij}\|) \right\rangle = \frac{V}{4\pi N_\beta r^2} \frac{dN_\beta(r)}{dr}, \quad (1)$$

we can obtain a measure of the structure of the liquid, which depends on temperature and density. Here,  $N_\alpha$  and  $N_\beta$  are the total number of nuclei of type  $\alpha$  and  $\beta$ , respectively that are contained in the volume  $V$ , while  $\vec{r}_{ij} = \vec{r}_i - \vec{r}_j$  is the separation between nuclei  $i$  and  $j$ .  $N_\beta(r)$  is the total number of nuclei of species  $\beta$  within a sphere of radius  $r$  around a nuclei of type  $\alpha$  [54,55]. This function,  $g_{\alpha\beta}(r)$ , can be interpreted as the probability of finding a particle of type  $\alpha$  at a distance  $r$  from a particle of type  $\beta$ .

In Fig. 2, we compare radial distribution functions of liquid magnesium over a wide range of temperatures and densities. For every density, we observe that the average distance to the nearest neighbor, given by the location of the first maximum of the  $g(r)$ , slightly decreases with increasing temperature. At  $6.89 \text{ g cm}^{-3}$ , this distance shifts from  $1.9 \text{ \AA}$  at  $20\,000 \text{ K}$  to  $1.8 \text{ \AA}$  at  $100\,000 \text{ K}$ . This 5% decrease is caused by stronger collisions and higher kinetic energy. As expected, the distance to the nearest neighbors depends strongly on density. At the highest density explored ( $51.67 \text{ g cm}^{-3}$ ), this distance decreased to  $0.96 \text{ \AA}$ . This value does not depend much on temperature.

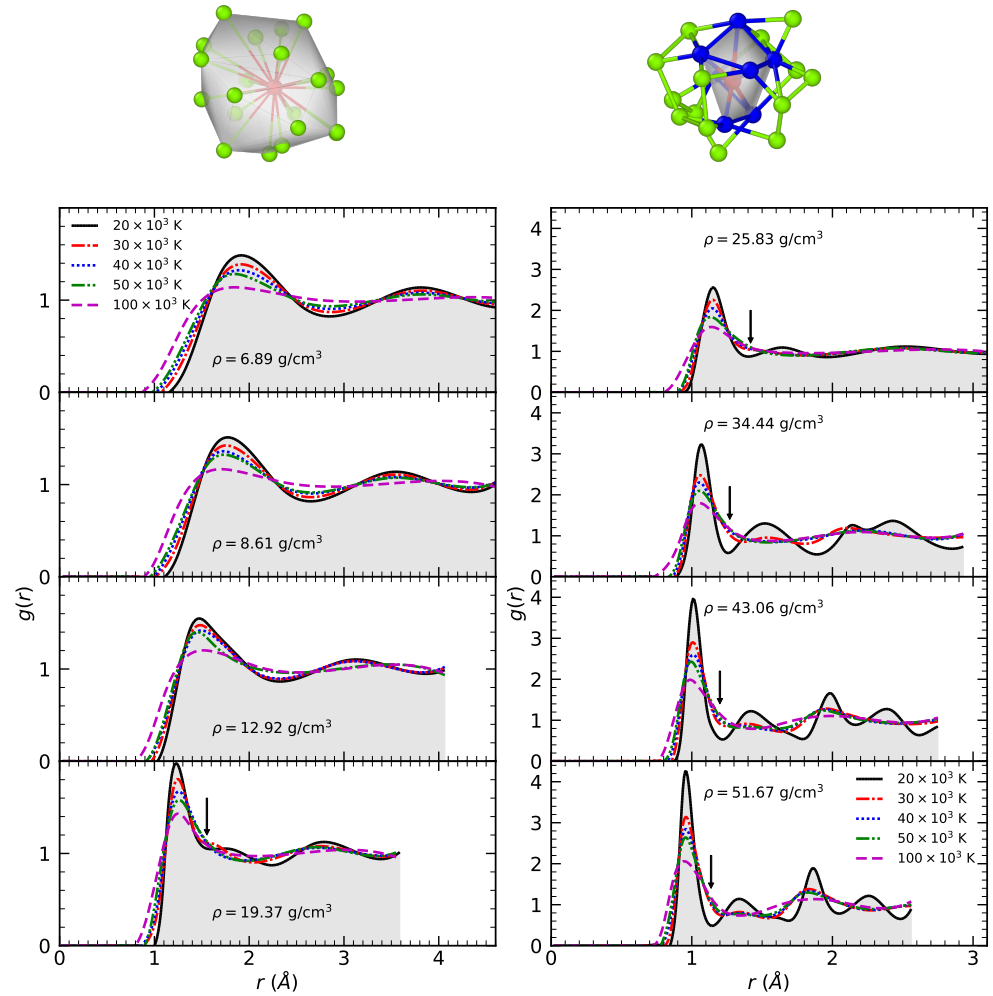


**Figure 2.** Radial distribution function of liquid elemental magnesium at 8 different densities as a function of temperature. The diagrams on the top correspond to the typical environment of a magnesium atom: surrounded by an average of 18 nearest neighbors within  $2.39 \text{ \AA}$  at  $12.92 \text{ g cm}^{-3}$  and  $20\,000 \text{ K}$  (left), and surrounded by a closer shell of only 6 to 7 neighboring atoms at  $25.83 \text{ g cm}^{-3}$  and  $20\,000 \text{ K}$ . For the three highest densities in our simulations ( $\rho \geq 34.44 \text{ g cm}^{-3}$ ), the system freezes into a simple cubic structure at  $20\,000 \text{ K}$ , which corresponds to the stable phase of Mg observed experimentally at pressures exceeding  $1 \text{ TPa}$ , the highest pressures ever reported in experiments of Mg to date [56]. The arrows indicate the location of an emerging intermediate local minimum.

We can also observe in Fig. 2 that the shape of the all  $g(r)$  curves at a low densities is fairly similar. All curves have two well-defined maxima and two minima. However, for densities of  $19.37 \text{ g cm}^{-3}$  and higher, the liquid becomes significantly more structured. The curve develops an additional intermediate local maxima that result in a new local minimum at  $\sim 1.55 \text{ \AA}$ . As density increases, this intermediate maximum becomes more pronounced. In our simulations at  $20\,000 \text{ K}$ , the system freezes into the simple cubic phase

for densities of  $34.44 \text{ g cm}^{-3}$  and higher, which corresponds to pressures higher than 24381 GPa. This simple cubic phase has been observed experimentally at pressures of 1 TPa [56]. With crystal structure search methods, a series of other high-pressure structures including body-centered cubic, face-centered cubic, and simple hexagonal and simple cubic phases have been predicted for magnesium [57]. When this crystallization happens in our MD simulations, the subtle features of the liquid  $g(r)$  functions become amplified. But for temperatures of 30 000 K and above, we found that the system remained in a liquid state for all densities. Still the local minimum at  $r_{\min} \sim 1.55 \text{ \AA}$  persisted. We will discuss these changes in terms of the atomic coordination number in the next section.

### 3.2. Coordination Number

A further measure of the structure of the liquid is the coordination number, given by

$$C_{\alpha\beta} = \frac{4\pi N_{\beta}}{V} \int_0^{r_{\min}} r^2 g_{\alpha\beta}(r) dr \quad (2)$$

where  $C_{\alpha\beta}$  is defined to be the number of atoms of type  $\beta$  that are within a spherical region of radius  $r_{\min}$ , centered at an atom of species  $\alpha$  [54]. Here, we adopted the usual convention that  $r_{\min}$  is the location of the first minimum of the radial distribution functions  $g_{\alpha\beta}(r)$ . The integrated nucleus-nucleus pair correlation function, given by  $N_{\beta}(r)$  in Eq. (1), can be employed to define a coordination number in Eq. (2) when evaluated at the location of the first minimum, that is,  $N_{\beta}(r_{\min}) = C_{\alpha\beta}$ .

In Fig. 3, we show the radial distribution functions of liquid elemental magnesium at 30 000 K and the corresponding integrated nucleus-nucleus pair correlation functions,  $N(r)$ . The shaded areas in the top panel highlights the interval  $[0, r_{\min}]$  over which the integration in Eq. (2) is performed. As density increases, the position of the first local maximum shifts to smaller distances and the peak becomes narrower, which indicates that the distance to first neighbors is decreasing.  $r_{\min}$ , also decreases with increasing density, reducing the total area below the curve and, hence, the coordination number.

As the atoms get closer, the liquid develops a new structure, which is reflected in the intermediate local maximum that starts developing in the  $g(r)$  for densities higher than  $25.83 \text{ g cm}^{-3}$  at 30 000 K, as we can see in Fig. 3, which corresponds to a pressure of 13147 GPa. The typical environment of a magnesium atom, after this intermediate local maximum develops, is shown at the top of Fig. 2, where a new shell of nearest neighbors forms. The slope  $(dE/d\rho)_T$  is positive, therefore pressure ionization is likely to take place [23]. As described in the previous section, a transition occurs in the liquid for higher densities, where a new intermediate maximum appears, which abruptly decreases the value of  $r_{\min}$  and, hence, the coordination number.

In Fig. 4, we show the resulting Mg-Mg coordination number in liquid magnesium for a wide range of temperatures and densities. As we can observe in the figure, the coordination number first increases from 14 to 18 at  $T = 20\,000 \text{ K}$  and then abruptly drops to 7, consistent with the diagram shown in Fig. 2. Something similar occurs at  $T = 30\,000 \text{ K}$ , where the coordination number drops from 18 to 8. This is an indication that the system prefers a coordination similar to the simple cubic structure, where the coordination number is 6. For higher temperatures, this intermediate maximum never develops for this range of densities, but it is likely to appear for  $\rho > 60 \text{ g cm}^{-3}$ . For  $T > 30\,000 \text{ K}$ , the coordination number remains between 13 and 18 at all densities.

### 3.3. Electronic Density of states

We also identified changes in the electronic structure of Mg at conditions where structure of the liquid changes and the new intermediate  $g(r)$  maximum appears. At ultrahigh pressure, solid magnesium has been predicted to assume an electricle structure [56–58]. In Fig. 5, we show the electronic density of occupied states (DOS) together with the electronic localization function (ELF) for liquid Mg at 30 000 K. In the DOS, we observe with increasing density a clear broadening of the 2s and 2p energy bands and a shift of

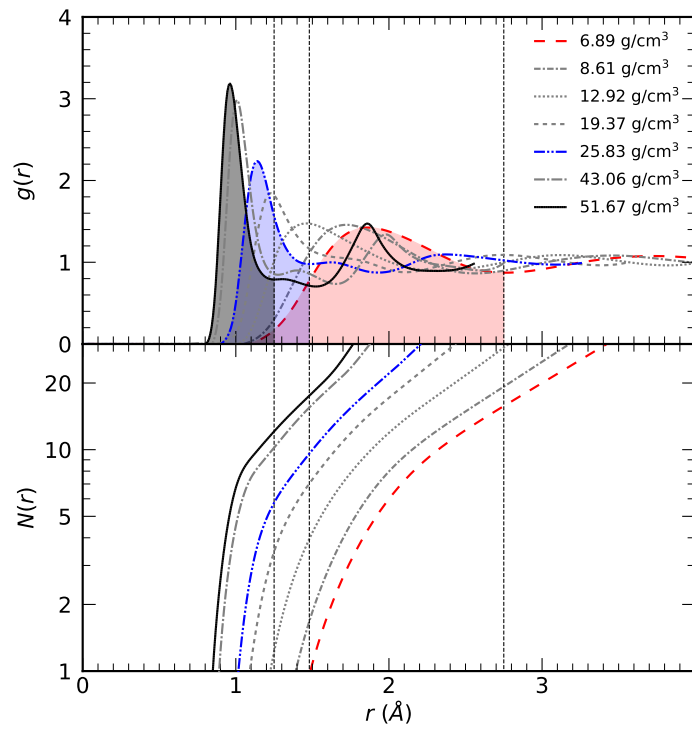


**Figure 3.** Radial distribution functions,  $g(r)$ , of liquid Mg at  $T = 30000$  K (top panel) and the corresponding integrated nucleus-nucleus pair correlation functions,  $N(r)$  (bottom panel). For densities higher than  $25.83 \text{ g cm}^{-3}$ , the  $g(r)$  function develops an intermediate maximum, which decreases the area below the curves and, consequently, the coordination number. The vertical bars indicate the location of the first minimum for the highlighted  $g(r)$  functions, corresponding to  $6.89$ ,  $25.83$ , and  $51.67 \text{ g cm}^{-3}$ .

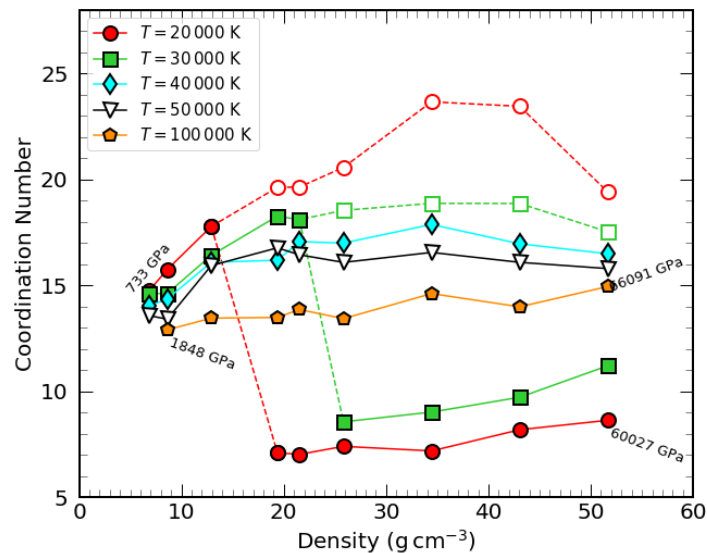


**Figure 4.** Coordination number  $C_{\text{Mg-Mg}}$  of liquid magnesium as a function of density for five different temperatures. For densities higher than  $25.83 \text{ g cm}^{-3}$ , the  $g(r)$  function develops an intermediate maximum, which increases the coordination number. The labels next to the symbols in the right panel indicate the pressure of selected simulations, and the open symbols indicate the coordination number obtained if we ignore the intermediate minimum and perform the integration in Eq. (2) up to the next local minimum.

the eigenvalues towards lower energies. This broadening does not affect the electrons in the conduction band (3s) in a significant way. However, at  $21.53 \text{ g cm}^{-3}$ , the broadening of the other bands is significant and almost closes the gap between the 2s and 2p bands. According to Ref. [33], these conditions fall in the regime of pressure ionization where the effects of thermal ionization are expected to be small. The ELF depicts location of electronic charge in the between void between the nuclei, which is the typical electrider behavior that results from the repulsion of core electrons. For the simple cubic phase of Mg, this has recently been reported by a experimental-theoretical study [56]. With *ab initio* methods, this has been predicted to occur in many solid structures at high pressure [59]. In Fig. 5, we show that also the Mg liquid exhibits electrider behavior, which shares similarities to earlier predictions for liquid iron [60].

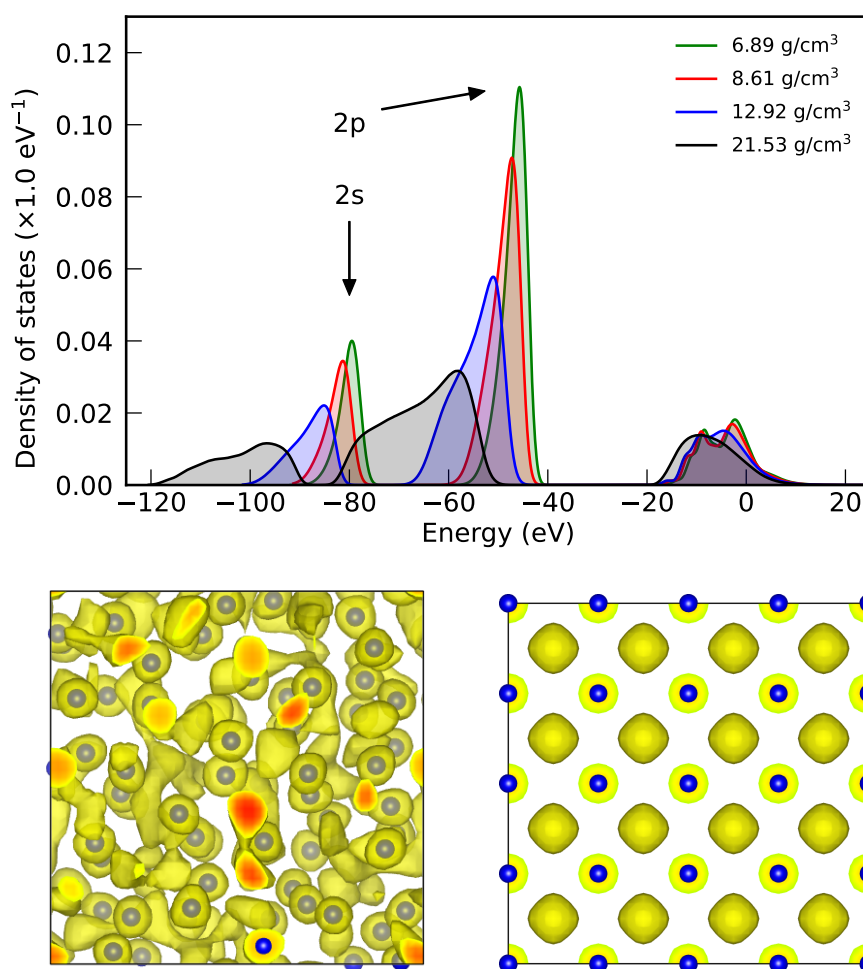


**Figure 5.** Top: Electronic density of occupied states of Mg based on our DFT-MD simulations at different densities for a temperature of 30 000 K. The energies of all MD configurations were shifted so that the Fermi energies are aligned at  $E = 0 \text{ eV}$ . Bottom: ELF function of liquid (left) and solid Mg in the simple cubic phase (right) at  $25.83 \text{ g cm}^{-3}$ . In the solid phase (right), the electronic charge (yellow pockets) is localized in the voids between the nuclei, which depicts the typical electrider behavior that has been predicted with *ab initio* method to occur in many solid structures including K [58,61,62] and Mg [56]. Here we also find the Mg liquid to exhibit electrider behavior (left), which has been predicted to occur in liquid Fe [60].

### 3.4. MgO and MgSiO<sub>3</sub>

We do not observe an intermediate maximum or similar structural change in our simulations of MgO. In Fig. 6, we plot the radial distribution functions (left panel) of MgO which show that the peaks becomes more pronounced with increasing density, but there

is no significant change in the topology of these functions as we observed in elemental Mg, indicating that the structure of the liquid varies smoothly with both temperature and density. At densities of  $24.99 \text{ g cm}^{-3}$  and higher, the Mg-Mg and O-O coordination increases, as shown by the separation of the radial distribution function in two distinctive peaks that separates the first nearest neighbors from the second nearest neighbors.

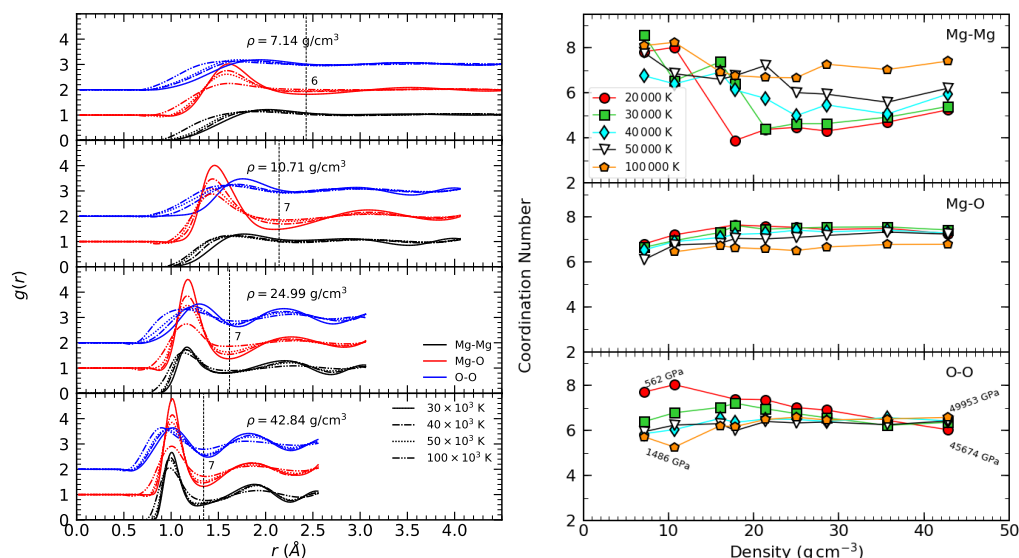


**Figure 6.** Coordination number of liquid MgO (right panel) as a function of density for five different temperatures. The radial distribution functions of MgO (left panel) show the location of the first local minimum (vertical bars for Mg-O), used to calculate the coordination number using Eq. (2). The small number near the vertical bars indicate the Mg-O coordination number at that local minimum. The Mg-O and O-O  $g(r)$  functions have been shifted upwards for clarity. The four text labels in the lowest right panel indicate the pressure in the simulations at the lower and highest temperatures for two density values.

The Mg-Mg coordination number is much higher in liquid, elemental Mg ( $\sim 14$ ) than in liquid MgO. In the presence of oxygen, the Mg-Mg coordination number decreases from 8 to 4-6 with increasing density, as we observe in the right panel of Fig. 6. However, this lower coordination is comparable to that of elemental Mg ( $\sim 7-10$ ) if the density of that system is high and the temperature is low, as we showed in Fig. 4. The Mg-O coordination number was found to be around 7 for all temperatures and densities, consistent with previous studies of MgO at high temperatures and densities [19]. Similarly, the O-O coordination number remained approximately 6. This is smaller than the value found for the molecular fluid  $\text{GeO}_2$  liquid, where the average O-O coordination number was found to be around 9 and a Ge-O coordination number of 2 at 1500 K and low temperatures [63,64]. This is not the case of MgO, which behaves as an atomic fluid. This is comparable to silica, which is predicted to have a mixed coordination between the 6-fold coordinated pyrite-type phase and the 9-fold coordinated  $\text{Fe}_2\text{P}$ -type phase at high pressure [24]. Therefore, coordination numbers with oxygen between 6 and 9 are expected at these conditions.

In the case of  $\text{MgSiO}_3$ , the Mg-O coordination number is also between 6 and 8, as we can see in Fig. 7, but slightly larger than 8 at some densities. The Mg-Mg  $g(r)$  functions in the left panel show that magnesium atoms are not correlated, with no clear signature of a local minimum at most of the conditions that allows to identify a layer of first nearest neighbors. When the identification is possible, the Mg-Mg coordination number in  $\text{MgSiO}_3$  lies between 2 and 4. While the Mg-O coordination number seems to decrease with density, the Si-O coordination number increases with increasing density, regardless of the temperature, from 6 to 8. The O-O coordination number is larger in the  $\text{MgSiO}_3$  liquid than in the MgO liquid, reaching values between 7 to 9 in the latter case, while MgO



shows an average of 6 for most conditions. Regarding the distance to nearest neighbors, or bond length, we find that the Mg-O bond length is larger in MgSiO<sub>3</sub> than in MgO. For a comparable density of  $\sim 25 \text{ g cm}^{-3}$ , this distance is 1.3 Å in MgSiO<sub>3</sub>, while for MgO, this distance is about 1.2 Å. At all conditions, the Si-O bond length is smaller than the Mg-O, and both are larger than the O-O bond length. As in the case of MgO, there no signature of an abrupt structure transition, as we observed in pure Mg.

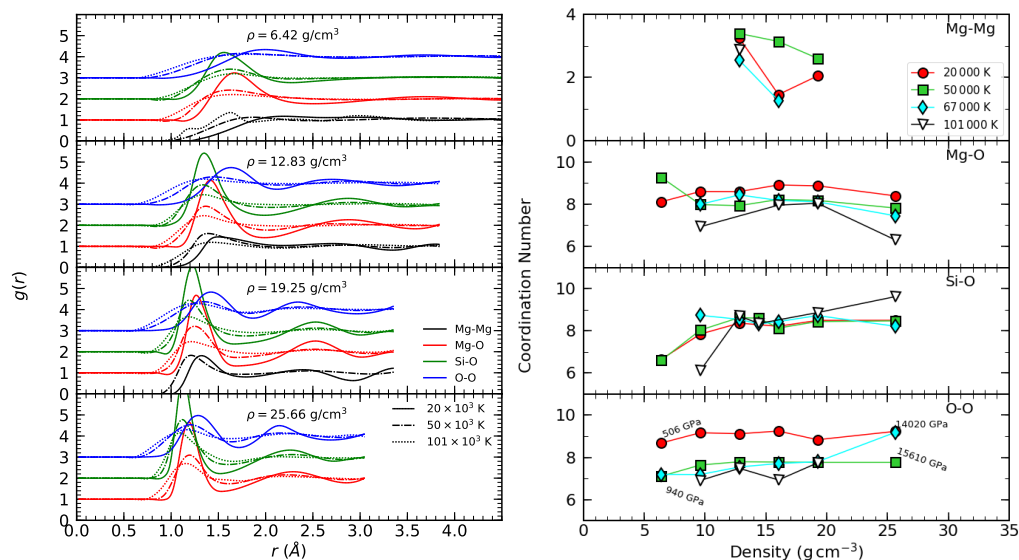


**Figure 7.** Coordination number of liquid MgSiO<sub>3</sub> (right panel) as a function of density for four different temperatures. The radial distribution functions of MgSiO<sub>3</sub> (left panel) show the location of the first local minimum, used to calculate the coordination number using Eq. (2). The Mg-O, Si-O, and O-O  $g(r)$  functions have been shifted upwards for clarity. The text labels on top of the symbols of the right panel indicate the pressure of the sample at the corresponding density and temperature.

#### 4. Conclusions

We have studied the structural properties of magnesium liquids in a broad range of temperatures and densities using *ab initio* simulations. We found evidence of a structural transition in liquid Mg around  $20 \text{ g cm}^{-3}$ , where the emergence of a new intermediate maximum in the radial distribution function leads to an abrupt decrease in the coordination number with increasing density for low temperatures. The structural change in liquid elemental magnesium is an indication of a transition to electrone-type behavior, consistent with recent experimental finding of electrone phases of Mg at ultrahigh pressure [56]. This transition does not occur in the other magnesium liquids, MgO and MgSiO<sub>3</sub>, where compression introduces only gradual changes in the coordination. Under no conditions we found a signature of a stable molecular bond between Mg and O species. However, the Mg and O nuclei exhibit positive correlations that are stronger than those between the other pairs. The presence of silicon increases the O-O coordination number, which is larger in MgSiO<sub>3</sub> than in MgO. The Mg-O bond length is smaller in MgO when compared to MgSiO<sub>3</sub> at similar conditions, and it is always larger than the Si-O bond length within the same MgSiO<sub>3</sub> liquid. We did not observe the formation of any molecule, making Mg, MgO, and MgSiO<sub>3</sub> atomic fluids at the conditions studied.

**Funding:** This research was funded by NSF grant number PHY-2020249.

**Data Availability Statement:** The equation of state of Mg, MgO, and MgSiO<sub>3</sub> can be found in the supplementary material of Refs. [17,32,33], respectively.

**Acknowledgments:** This work was supported by the US National Science Foundation (PHY-2020249) as part of the Center for Matter at Atomic Pressures (CMAP). We thank V. N. Robinson for discussions on electrifieds.

**Conflicts of Interest:** The authors declare no conflict of interest.

## Abbreviations

The following abbreviations are used in this manuscript:

DFT-MD	Density Functional Theory Molecular Dynamics
PIMC	Path Integral Monte Carlo
VASP	Vienna Ab initio Simulation Package

## References

1. Labrosse, S.; Hernlund, J.; Coltice, N. A crystallizing dense magma ocean at the base of the Earth's mantle. *Nature* **2007**, *450*, 866–869.
2. Rogers, L.A. Most 1.6 earth-radius planets are not rocky. *Astrophysical Journal* **2015**, *801*, 41. <https://doi.org/10.1088/0004-637X/801/1/41>.
3. Kovačević, T.; González-Cataldo, F.; Stewart, S.T.; Militzer, B. Miscibility of rock and ice in the interiors of water worlds. *Scientific reports* **2022**, *12*, 1–11. <https://doi.org/https://doi.org/10.1038/s41598-022-16816-w>.
4. Kovačević, T.; González-Cataldo, F.; Militzer, B. The homogeneous mixing of MgO and H<sub>2</sub>O at extreme conditions. *Contributions to Plasma Physics* **2023**, p. e202300017. <https://doi.org/https://doi.org/10.1002/ctpp.202300017>.
5. Soubiran, F.; Militzer, B. Electrical conductivity and magnetic dynamos in magma oceans of Super-Earths. *Nature Communications* **2018**, *9*, 3883.
6. Boujibar, A.; Driscoll, P.; Fei, Y. Super-Earth Internal Structures and Initial Thermal States. *Journal of Geophysical Research: Planets* **2020**, *125*. <https://doi.org/10.1029/2019JE006124>.
7. Smith, R.F.; Eggert, J.H.; Jeanloz, R.; Duffy, T.S.; Braun, D.G.; Patterson, J.R.; Rudd, R.E.; Biener, J.; Lazicki, a.E.; Hamza, a.V.; et al. Ramp compression of diamond to five terapascals. *Nature* **2014**, *511*, 330–333.
8. Smith, R.F.; Fratanduono, D.E.; Braun, D.G.; Duffy, T.S.; Wicks, J.K.; Celliers, P.M.; Ali, S.J.; Fernandez-Pañella, A.; Kraus, R.G.; Swift, D.C.; et al. Equation of state of iron under core conditions of large rocky exoplanets. *Nature Astronomy* **2018**, *2*, 452–458. <https://doi.org/10.1038/s41550-018-0437-9>.
9. González-Cataldo, F.; Godwal, B.K.; Driver, K.; Jeanloz, R.; Militzer, B. Model of ramp compression of diamond from ab initio simulations. *Phys. Rev. B* **2021**, *104*, 134104. <https://doi.org/10.1103/PhysRevB.104.134104>.
10. Saumon, D.; Blouin, S.; Tremblay, P.E. Current challenges in the physics of white dwarf stars. *Physics Reports* **2022**, *988*, 1–63, [2209.02846]. <https://doi.org/10.1016/j.physrep.2022.09.001>.
11. Coppari, F.; Smith, R.F.; Wang, J.; Millot, M.; Kim, D.; Rygg, J.R.; Hamel, S.; Eggert, J.H.; Duffy, T.S. Implications of the iron oxide phase transition on the interiors of rocky exoplanets. *Nature Geoscience* **2021**, *14*, 121–126. <https://doi.org/10.1038/s41561-020-00684-y>.
12. Zurkowski, C.; Fei, Y. Mineralogy of Planetary Cores. In *Celebrating the International Year of Mineralogy: Progress and Landmark Discoveries of the Last Decades*; Springer, 2023; pp. 207–247.
13. Militzer, B.; Hubbard, W.B.; Wahl, S.; Lunine, J.I.; Galanti, E.; Kaspi, Y.; Miguel, Y.; Guillot, T.; Moore, K.M.; Parisi, M.; et al. Juno Spacecraft Measurements of Jupiter's Gravity Imply a Dilute Core. *The Planetary Science Journal* **2022**, *3*, 185. <https://doi.org/10.3847/PSJ/ac7ec8>.
14. González-Cataldo, F.; Wilson, H.F.; Militzer, B. Ab Initio Free Energy Calculations of the Solubility of Silica in Metallic Hydrogen and Application To Giant Planet Cores. *The Astrophysical Journal* **2014**, *787*, 79.
15. Abu-Shawareb, H.; Acree, R.; Adams, P.; Adams, J.; Addis, B.; Aden, R.; Adrian, P.; Afeyan, B.; Aggleton, M.; Aghaian, L.; et al. Lawson criterion for ignition exceeded in an inertial fusion experiment. *Physical Review Letters* **2022**, *129*, 075001.
16. de Koker, N.; Stixrude, L. Self-consistent thermodynamic description of silicate liquids, with application to shock melting of MgO periclase and MgSiO<sub>3</sub> perovskite. *Geophysical Journal International* **2009**, *178*, 162–179.
17. González-Cataldo, F.; Soubiran, F.; Peterson, H.; Militzer, B. Path integral Monte Carlo and density functional molecular dynamics simulations of warm dense MgSiO<sub>3</sub>. *Physical Review B* **2020**, *101*, 024107. <https://doi.org/10.1103/PhysRevB.101.024107>.
18. Stixrude, L.; Scipioni, R.; Desjarlais, M.P. A silicate dynamo in the early Earth. *Nature Communications* **2020**, *11*, 935. <https://doi.org/10.1038/s41467-020-14773-4>.
19. Karki, B.B.; Bhattarai, D.; Stixrude, L. First-principles calculations of the structural, dynamical, and electronic properties of liquid MgO. *Physical Review B* **2006**, *73*, 174208. <https://doi.org/10.1103/PhysRevB.73.174208>.
20. Karki, B.B.; Bhattarai, D.; Stixrude, L. First-principles simulations of liquid silica: Structural and dynamical behavior at high pressure. *Physical Review B* **2007**, *76*, 104205. <https://doi.org/10.1103/PhysRevB.76.104205>.
21. González-Cataldo, F.; Davis, S.; Gutiérrez, G. Z method calculations to determine the melting curve of silica at high pressures. In *Proceedings of the Journal of Physics: Conference Series*. IOP Publishing, 2016, Vol. 720, p. 012032.

22. Mookherjee, M.; Stixrude, L.; Karki, B. Hydrous silicate melt at high pressure. *Nature* **2008**, *452*, 983–986. <https://doi.org/10.1038/nature06918>. 305
23. González-Cataldo, F.; Militzer, B. Thermal and pressure ionization in warm, dense MgSiO<sub>3</sub> studied with first-principles computer simulations. *AIP Conference Proceedings* **2020**, *2272*, 090001. <https://doi.org/10.1063/12.0000793>. 306
24. Liu, C.; Shi, J.; Gao, H.; Wang, J.; Han, Y.; Lu, X.; Wang, H.t.; Xing, D.; Sun, J. Mixed Coordination Silica at Megabar Pressure. *Physical Review Letters* **2021**, *126*, 035701. <https://doi.org/10.1103/PhysRevLett.126.035701>. 307
25. Ceperley, D.M. Fermion nodes. *Journal of Statistical Physics* **1991**, *63*, 1237–1267. 308
26. Ceperley, D.M. Path integrals in the theory of condensed helium. *Rev. Mod. Phys.* **1995**, *67*, 279–355. <https://doi.org/10.1103/RevModPhys.67.279>. 309
27. Ceperley, D. Path integral Monte Carlo methods for fermions. In *Monte Carlo and Molecular Dynamics of Condensed Matter Systems*; Binder, K.; Ciccotti, G., Eds.; Editrice Compositori, Bologna, Italy, 1996; Vol. 49, p. 443. 310
28. Car, R.; Parrinello, M. Unified Approach for Molecular Dynamics and Density-Functional Theory. *Phys. Rev. Lett.* **1985**, *55*, 2471–2474. <https://doi.org/10.1103/PhysRevLett.55.2471>. 311
29. Payne, M.C.; Teter, M.P.; Allan, D.C.; Arias, T.A.; Joannopoulos, J.D. Iterative minimization techniques for ab initio total-energy calculations: molecular dynamics and conjugate gradients. *Rev. Mod. Phys.* **1992**, *64*, 1045–1097. <https://doi.org/10.1103/RevModPhys.64.1045>. 312
30. Marx, D.; Hutter, J. *Ab initio molecular dynamics: basic theory and advanced methods*; Cambridge University Press, 2009. 313
31. Driver, K.P.; Soubiran, F.; Militzer, B. Path integral Monte Carlo simulations of warm dense aluminum. *Phys. Rev. E* **2018**, *97*, 063207. 314
32. Soubiran, F.; González-Cataldo, F.; Driver, K.P.; Zhang, S.; Militzer, B. Magnesium oxide at extreme temperatures and pressures studied with first-principles simulations. *The Journal of Chemical Physics* **2019**, *151*, 214104. <https://doi.org/10.1063/1.5126624>. 315
33. González-Cataldo, F.; Soubiran, F.; Militzer, B. Equation of state of hot, dense magnesium derived with first-principles computer simulations. *Physics of Plasmas* **2020**, *27*, 092706. <https://doi.org/10.1063/5.0017555>. 316
34. Driver, K.P.; Militzer, B. First-principles simulations of warm dense lithium fluoride. *Phys. Rev. E* **2017**, *95*, 043205. 317
35. Zhang, S.; Militzer, B.; Gregor, M.C.; Caspersen, K.; Yang, L.H.; Gaffney, J.; Ogitsu, T.; Swift, D.; Lazicki, A.; Erskine, D.; et al. Theoretical and experimental investigation of the equation of state of boron plasmas. *Phys. Rev. E* **2018**, *98*, 023205. 318
36. Driver, K.P.; Soubiran, F.; Zhang, S.; Militzer, B. First-principles equation of state and electronic properties of warm dense oxygen. *J. Chem. Phys.* **2015**, *143*, 164507. 319
37. Militzer, B.; Driver, K.P. Development of Path Integral Monte Carlo Simulations with Localized Nodal Surfaces for Second-Row Elements. *Phys. Rev. Lett.* **2015**, *115*, 176403. 320
38. Driver, K.P.; Soubiran, F.; Zhang, S.; Militzer, B. Comparison of path integral Monte Carlo simulations of helium, carbon, nitrogen, oxygen, water, neon, and silicon plasmas. *High Energy Density Physics* **2017**, *23*, 81–89. 321
39. Zhang, S.; Militzer, B.; Benedict, L.X.; Soubiran, F.; Sterne, P.A.; Driver, K.P. Path integral Monte Carlo simulations of dense carbon-hydrogen plasmas. *J. Chem. Phys.* **2018**, *148*, 102318. 322
40. Wilson, H.F.; Wong, M.L.; Militzer, B. Superionic to Superionic Phase Change in Water: Consequences for the Interiors of Uranus and Neptune. *Phys. Rev. Lett.* **2013**, *110*, 151102. 323
41. Millot, M.; Hamel, S.; Rygg, J.R.; Celliers, P.M.; Collins, G.W.; Coppari, F.; Fratanduono, D.E.; Jeanloz, R.; Swift, D.C.; Eggert, J.H. Experimental evidence for superionic water ice using shock compression. *Nature Physics* **2018**, *14*, 297–302. 324
42. Militzer, B. Path Integral Monte Carlo Simulations of Hot Dense Hydrogen. PhD thesis, University of Illinois at Urbana-Champaign, 2000. 325
43. Kresse, G.; Furthmüller, J. Efficient iterative schemes for ab initio total-energy calculations using a plane-wave basis set. *Phys. Rev. B* **1996**, *54*, 11169. 326
44. Blöchl, P.E. Projector augmented-wave method. *Phys. Rev. B* **1994**, *50*, 17953–17979. 327
45. Kresse, G.; Joubert, D. From ultrasoft pseudopotentials to the projector augmented-wave method. *Phys. Rev. B* **1999**, *59*, 1758–1775. 328
46. Perdew, J.P.; Burke, K.; Ernzerhof, M. Generalized Gradient Approximation Made Simple. *Phys. Rev. Lett.* **1996**, *77*, 3865–3868. 329
47. Mehta, S.; Price, G.; Alfè, D. Ab initio thermodynamics and phase diagram of solid magnesium: A comparison of the LDA and GGA. *The Journal of chemical physics* **2006**, *125*, 194507. 330
48. Driver, K.P.; Militzer, B. First-principles simulations and shock Hugoniot calculations of warm dense neon. *Phys. Rev. B* **2015**, *91*, 045103. 331
49. Militzer, B.; González-Cataldo, F.; Zhang, S.; Driver, K.P.; Soubiran, F. First-principles equation of state database for warm dense matter computation. *Physical Review E* **2021**, *103*, 013203. <https://doi.org/10.1103/PhysRevE.103.013203>. 332
50. McCoy, C.A.; Marshall, M.C.; Polsin, D.N.; Fratanduono, D.E.; Celliers, P.M.; Meyerhofer, D.D.; Boehly, T.R. Hugoniot, sound velocity, and shock temperature of MgO to 2300 GPa. *Phys. Rev. B* **2019**, *100*, 014106. 333
51. Root, S.; Shulenburg, L.; Lemke, R.W.; Dolan, D.H.; Mattsson, T.R.; Desjarlais, M.P. Shock Response and Phase Transitions of MgO at Planetary Impact Conditions. *Physical Review Letters* **2015**, *115*, 198501. <https://doi.org/10.1103/PhysRevLett.115.198501>. 334
52. Fratanduono, D.E.; Millot, M.; Kraus, R.G.; Spaulding, D.K.; Collins, G.W.; Celliers, P.M.; Eggert, J.H. Thermodynamic properties of MgSiO<sub>3</sub> at super-Earth mantle conditions. *Phys. Rev. B* **2018**, *97*, 214105. 335

53. Militzer, B.; González-Cataldo, F.; Zhang, S.; Whitley, H.D.; Swift, D.C.; Millot, M. Nonideal mixing effects in warm dense matter studied with first-principles computer simulations. *The Journal of Chemical Physics* **2020**, *153*, 184101. <https://doi.org/10.1063/5.0023232>. 362
54. Karki, B.B.; Ghosh, D.B.; Bajgain, S.K. Simulation of Silicate Melts Under Pressure. In *Magmas Under Pressure*; Elsevier, 2018; pp. 419–453. <https://doi.org/10.1016/B978-0-12-811301-1.00016-2>. 363
55. Allen, M.; Tildesley, D. *Computer Simulation of Liquids*; Oxford University Press: New York, 1987. 364
56. Gorman, M.G.; Elatresh, S.; Lazicki, A.; Cormier, M.M.E.; Bonev, S.A.; McGonegle, D.; Briggs, R.; Coleman, A.L.; Rothman, S.D.; Peacock, L.; et al. Experimental observation of open structures in elemental magnesium at terapascal pressures. *Nature Physics* **2022**, *18*, 1307–1311. <https://doi.org/10.1038/s41567-022-01732-7>. 365
57. Li, P.; Gao, G.; Wang, Y.; Ma, Y. Crystal structures and exotic behavior of magnesium under pressure. *The Journal of Physical Chemistry C* **2010**, *114*, 21745–21749. 366
58. Zong, H.; Robinson, V.N.; Hermann, A.; Zhao, L.; Scandolo, S.; Ding, X.; Ackland, G.J. Free electron to electrone transition in dense liquid potassium. *Nature Physics* **2021**, *17*, 955–960. 367
59. Miao, M.S.; Hoffmann, R. High pressure electrides: a predictive chemical and physical theory. *Accounts of chemical research* **2014**, *47*, 1311–1317. 368
60. Dai, J.; Kang, D.; Zhao, Z.; Wu, Y.; Yuan, J. Dynamic ionic clusters with flowing electron bubbles from warm to hot dense iron along the Hugoniot curve. *Physical Review Letters* **2012**, *109*, 175701. 369
61. Woolman, G.; Robinson, V.N.; Marqués, M.; Loa, I.; Ackland, G.J.; Hermann, A. Structural and electronic properties of the alkali metal incommensurate phases. *Physical Review Materials* **2018**, *2*, 053604. 370
62. Ayrinhac, S.; Robinson, V.N.; Decremps, F.; Gauthier, M.; Antonangeli, D.; Scandolo, S.; Morand, M. High-pressure transformations in liquid rubidium. *Physical Review Materials* **2020**, *4*, 113611. 371
63. Gutiérrez, G.; Rogan, J. Structure of liquid GeO<sub>2</sub> from a computer simulation model. *Physical Review E* **2004**, *69*, 031201. <https://doi.org/10.1103/PhysRevE.69.031201>. 372
64. Gutiérrez, G.; Menéndez-Proupin, E.; Loyola, C.; Peralta, J.; Davis, S. Computer simulation study of amorphous compounds: structural and vibrational properties. *Journal of Materials Science* **2010**, *45*, 5124–5134. <https://doi.org/10.1007/s10853-010-4579-0>. 373

**Disclaimer/Publisher's Note:** The statements, opinions and data contained in all publications are solely those of the individual author(s) and contributor(s) and not of MDPI and/or the editor(s). MDPI and/or the editor(s) disclaim responsibility for any injury to people or property resulting from any ideas, methods, instructions or products referred to in the content. 374  
375  
376  
377  
378  
379  
380  
381  
382  
383  
384  
385  
386  
387  
388  
389